Deformation Behavior of a Poly(ether ester) Copolymer. Quantitative Analysis of SAXS Fiber Patterns

Norbert Stribeck,*,† Stoyko Fakirov,‡ and Diana Sapoundjieva‡

Institut für Technische und Makromolekulare Chemie, Universität Hamburg, 20146 Hamburg, Germany, and Laboratory on Structure and Properties of Polymers, University of Sofia, 1126 Sofia, Bulgaria

Received November 30, 1998; Revised Manuscript Received February 10, 1999

ABSTRACT: A method for the quantitative analysis of two-dimensional small-angle X-ray scattering (SAXS) patterns with fiber symmetry is proposed and applied to a series of images recorded during straining and relaxation cycles of a two-phase polymer sample at a synchrotron beamline.The studied longitudinal scattering originates from microfibrils or lamellar stacks built from alternating soft and hard domains. The scattering intensity of the patterns is projected onto the direction of strain, yielding one-dimensional scattering curves. From these curves, interface distribution functions are computed and analyzed using an advanced stacking model with a small set of parameters. Not only the average domain heights but also four parameters characterizing each of two height distributions (hard and soft domains) are determined as a function of elongation. These parameters are norm, mean, variance, and skewness. They describe the response of the filled elastic network to strain.For the studied poly(ester ether) thermoplastic elastomer, the quantitative analysis shows that two microfibrillar components (an intact and a damaged one) can be identified in the patterns from samples at medium elongation as well as in patterns recorded during relaxation from medium elongation. Although the scattering patterns differ considerably, the hard domain distributions extracted from the fits are identical. The difference between elongated and relaxed state is in the distribution of the soft domain heights. There are indications for a nonuniform elasticity of the soft domains. The average internal strain of the soft domains can be computed and compared to the external strain; and pull out of tie molecules taut among different microfibrils can be studied.

1. Introduction

Structural changes on a nanometer scale, which take place in semicrystalline or other two-phase polymer materials during fiber spinning or straining can only be studied by those few methods which are minimally invasive with respect to materials processing. One of these methods is small-angle X-ray scattering (SAXS). By utilizing a powerful source (synchrotron beam) and a high-resolution two-dimensional detector, it is possible to record a series of detailed scattering patterns with high accuracy during short exposure times. Quite often, one observes fiber patterns with many reflections, which vary considerably as a function of tunable processing parameters.[1−4]

Even from two-dimensional (2D) patterns, the maximum accumulated counts of which range in the thousands, one can extract structural information by simply studying peak positions and other general features of the scattering patterns as a function of processing parameters. If, moreover, the number of accumulated counts per pixel exceeds 10 000, it becomes both a challenging and promising task to perform a quantitative analysis of the patterns by successive information extraction and late modeling. As a result of this procedure, one will gain information not only on long periods but also on domain sizes and domain size distributions. For a strained poly(ether ester) thermoplastic elastomer this means, e.g., that we should be able to extract the distributions of hard- and soft-domain heights as a function of elongation.

To simplify the task, we will fall back on Bonart's[1] proposal to split the information content of a fiber pattern into a longitudinal structure and a transverse structure, each of which is represented by a different projection of the fiber pattern. These projections are curves generated by certain integrals of the measured patterns and carefully chosen to represent different aspects of the 3D structure.

A demonstration of the quantitative analysis of a transverse structure from a straining series has been given elsewhere.[5] Here, we focus on the quantitative analysis of a longitudinal structure from a sample series, the qualitative analysis of which has already been published previously.[6]

The present study deals with projections onto the straining direction (longitudinal structure). Following a concept of Ruland,[7,8] the resulting curves are not fitted by a complex model but are analyzed step by step in order to "peel off" information. Finally, an interface distribution function (IDF)[9,10] is computed and analyzed utilizing a model which has been proposed earlier[8] and merges the well-known one-dimensional (1D) stacking model[11] and the model of homogeneous long period distributions.[10,12,13]

Although the proposed evaluation procedure is applicable in general, it may be inadequate if the effect of an orientation distribution becomes apparent in the scattering pattern. In this case, one should first try to determine the orientation distribution of the microfibrillar or lamellar stacks, as has been proposed by Murthy et al.[14,15] After that, one should be able to eliminate the effect of the orientation distribution in the scattering pattern utilizing a method proposed by Ruland.[16] Finally, the resulting pattern may be analyzed by the

† Universität Hamburg.
‡ University of Sofia.

10.1021/ma9818477 CCC: $18.00
Published on Web 04/24/1999

method proposed here.

In many papers, intensity cuts are analyzed. On the basis of basic scattering theory, it is readily established that such sections are related to a projected correlation function in real space. This means that any analysis based on intensity cuts is done under the premise that it makes sense to integrate (e.g., to smear) the structural information over planes perpendicular to the chosen direction of the cut. On the other hand, intensity projection analysis is frequently disliked for practical reasons. The argument put forward says that it is possible to have two- and four-point patterns which result in the same intensity distribution when projected along the fiber axis. This objection is not well-founded, because it is based on the erroneous implication that projection analysis would claim to fully characterize oriented structures. By contrast, intensity projection analysis studies intersections of the correlation function, and if two structures result in the same projected intensity, they do share the same intersection of their correlation functions in the fiber direction. It is just this structural aspect, which describes the correlations among the domains taken in the fiber direction, that to us is generally the most important feature of fiber structure to be related to materials performance. Therefore, we propose this analysis.

Another objection put forward is related to the description of the structure by parameters which consider an imperfection of the polymer domain structure. It is believed that parameters other than the average long period and domain heights could be chosen arbitrarily. We do not claim that there is no other structural model which might be able to fit the SAXS data. However, we claim that it is impossible to fit scattering data from polymers with a model that is based on well-defined domain heights only. An attempt to fit polymer structural data by a perfect lattice has never been successful, although interpretation of scattering data in terms of such simplified notion is ubiquitous. So, when searching for a model to fit scattering data, we recall the well-known fact that polymer structures are imperfect in general, and so we choose the obvious minimum parameter set. To date, we have gained methods and computing power which enable us to give special emphasis to imperfection in analysis. So if we are willing to undergo the effort, we no longer need to carry out SAXS analysis of polymers by zero-order approximations which are valid for well-ordered systems only. The well-informed reader might want to find comparison with the correlation function analysis method proposed by Vonk.[17,18] Correlation functions computed from the studied scattering patterns lack the specific features which must be observed in order to carry out the Vonk analysis. However, for different material, such comparison has been undertaken and published previously[19] with the finding that average domain heights coincide in the case of narrow domain height distributions. As soon as the domain height distributions grow broad, the correlation function becomes nonspecific and needs biased interpretation. Correlation functions from the studied poly(ether ester) sample neither exhibit a region of constant slope nor a clear floor level. According to private communication,[20] this is a general problem with poly(ether ester) material.

2. Theoretical Section

2.1 Definitions. Let $I(\vec{s})/V$ be the measurable SAXS intensity, normalized with respect to the irradiated volume, V. Let the magnitude of the scattering vector be defined by $|\vec{s}| = (2/\lambda) \sin \theta$, with λ being the wavelength of radiation and 2θ the scattering angle. For the ease of notation and because the treatment of absolute intensities is not intended here, let us write $I(\vec{s})$ for the normalized intensity.

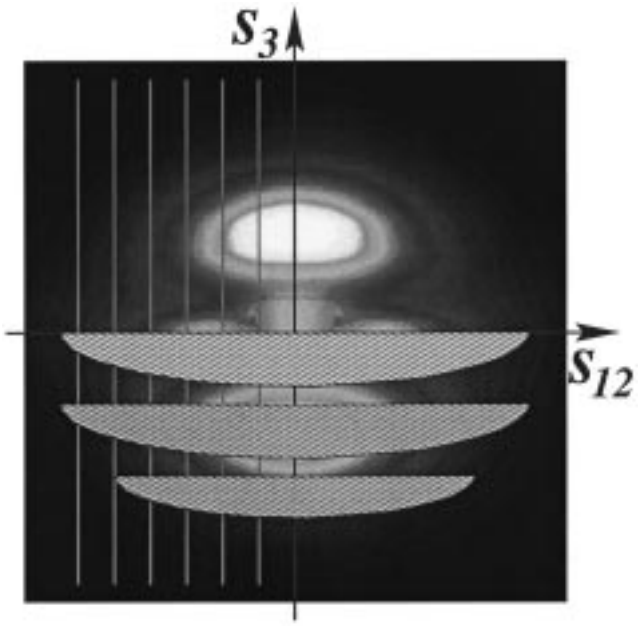

Figure 1. SAXS fiber pattern of an elongated PEE sample. Fiber axis is in s_3 direction. Vertical lines indicate the integration paths which generate the transverse projection studied in a previous paper. Horizontal disks indicate the integration planes which generate the longitudinal projection, $\{I\}_1(s_3)$, studied here.

In the case of a scattering pattern with fiber symmetry, it is convenient to write $I(\vec{s}) = I(s_{12},s_3)$ in cylindrical coordinates, with $s_{12} = \sqrt{s_1^2+s_2^2}$ and the component s_3 defining the symmetry axis of the pattern. If in the case of fiber symmetry the tangent plane approximation is assumed to be valid, the complete information of SAXS is in a 2D pattern, which can be recorded using a 2D detector.

2.2. Longitudinal Structure. Such small-angle fiber patterns may exhibit many reflections, and a modeling of the 2D pattern as a whole is expected to become cumbersome and prone to errors.

When dealing with fiber patterns in which orientation distributions do not play a predominant role, it appears suitable to extract what Bonart called "Längsstruktur" (longitudinal structure)[1] by computing the projection

$$\{I\}_1(s_3) = 2\pi \int_0^\infty s_{12} I(s_{12},s_3)\, \mathrm{d}s_{12} \qquad (1)$$

In Figure 1, several horizontal disks indicate planes of integration placed at different values of s_3. $\{I\}_1(s_3)$ is a one-dimensional scattering intensity which is related to the section $\lceil\gamma\rceil_1(x_3)$ of the correlation function $\gamma(\vec{x})$ in x_3 direction. Thus, it contains the information on only those chords passing the two-phase system in the direction parallel to the fiber axis, x_3. In Figure 2, we may represent such a chord by a deliberate vertical line. Traveling along such a line we will alternately move through the hard domain phase and the soft domain phase, from time to time crossing a phase boundary. Thus, structural parameters of physical interest are $\bar{d}_h$, the average travel distance inside the hard domain

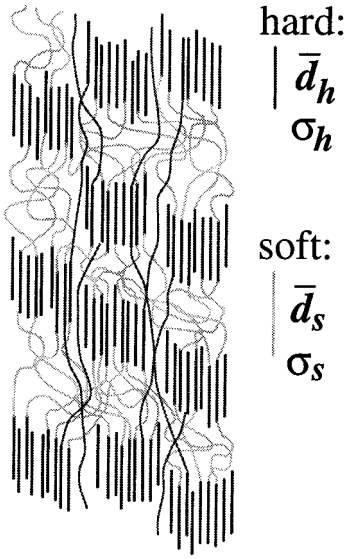

Figure 2. Sketch of a structure from hard- and soft domains oriented parallel to a fiber axis. $\{I\}_1(s_3)$, the projected curve extracted from the SAXS fiber pattern, is only sensitive to phase changes occurring when traveling in "vertical" direction.

phase, $\bar{d}_s$, the average travel distance inside the soft domain phase, and the variances (σ_h and σ_s) of their distributions, which shall be called domain height distributions $h_h(x_3)$ and $h_s(x_3)$.

To return to the relation between projection $\{I\}_1(s_3)$ and structure, more precisely,

$$F(\{I\}_1(s_3)) = Q\{\gamma\}_1(x_3) \tag{2}$$

the 1D Fourier transformation, F, of the projected intensity is the product from the invariant Q and the 1D section of the correlation function γ in the direction of the fiber axis. The intention of this work is the analysis of the 1D chord distribution, $g_1(x_3)$,

$$g_1(x_3) = f\frac{d^2\lceil\gamma\rceil_1(x_3)}{dx_3^2} \tag{3}$$

which is proportional to the second derivative of $\lceil\gamma\rceil_1(x_3)$. This function has been introduced by Ruland[9,21] and named the "interface distribution function" (IDF).

2.3. Porod's Law and Systematic Deviations. Because $\{I\}_1(s_3)$ describes a one-dimensional structure, similar to a "Lorentz corrected" curve from an isotropic pattern, it exhibits Porod's law with the scattering falling off with s_3^{-2}. Small deviations from the predicted falloff are attributed to the nonideal structure of the real two-phase system[7,22] and corrected accordingly, leading to the 1D interference function $G_1(s_3)$ of an ideal two-phase system

$$G_1(s_3) = \frac{(\{I\}_1(s_3) - I_{Fl})s_3^2}{\exp\left(-\frac{4}{9}\pi^2 w_t^2 s_3^2\right)} - A_{P_1} \tag{4}$$

A_{P_1}, Porod's asymptote of the projected SAXS intensity, is the constant governing Porod's law. The nonideal structure of the real two-phase system is described by I_{Fl} and w_t. Fluctuations of the electron density are considered by I_{Fl}, the density fluctuation background, which for practical reasons is assumed to be a constant. w_t is the width of the transition zone at the domain boundary, in which the density changes smoothly. A detailed description of the procedure established to determine the interference function follows in Data Evaluation.

2.4. IDF Analysis. *Basic Relation.* Using eqs 2−4 and the normalization $\int_{-\infty}^{\infty} g_1(x_3)\,dx_3 = A_{P_1}$, one finds that the IDF $g_1(x_3)$ is computed from $G_1(x_3)$ by a negative Fourier transformation

$$g_1(x_3) = -2\int_0^{\infty} G_1(s_3)\cos(2\pi s_3 x_3)\,ds_3 \tag{5}$$

As Ruland has shown,[9] $g_1(x_3)$ represents the distributions of chords from soft and hard domain phase and their correlations by an infinite series of distance distributions $h_i(x_3)$. This series starts with the two domain height distributions $h_h(x_3)$ and $h_s(x_3)$.

Choice of a Model. Assuming one-dimensional stacking statistics as defined by J. J. Hermans,[11] the IDF can be constructed from only $h_h(x_3)$ and $h_s(x_3)$. As has first been pointed out by Brämer,[23] stacking statistics overcomes the shortcoming of the one-dimensional paracrystalline model in which, for the case of considerable disorder, some adjacent motif domains penetrate each other. The second model frequently applied in order to fit one-dimensional statistics is that of a "homogeneous long period" (hL) distribution.[10,12,13] Here it is assumed that the structure is made from an ensemble of grains and every grain is of considerable size. Inside each grain, there is a perfect one-dimensional lattice, and only the lattice constant varies from grain to grain as defined by a heterogeneity distribution, $h_H(x_3)$. Its only parameter is its variance, σ_H, if Gaussian statistics is assumed. Both models have been merged by one of us.[8] It is found that the main effect of a $\sigma_H > 0$ is that the distributions $h_h(x_3)$ and $h_s(x_3)$ become asymmetric. Thus, we end up with a simple model with only six parameters based on Gaussian statistics, which may be interpreted in terms of either the two basic models (stacking and hL) or the asymmetric domain height distributions $h_h(x_3)$ and $h_s(x_3)$. The parameters of such a model are the area under both of the distributions, $W \approx A_{P_1}/2$; the average domain heights of the hard and the soft domain phase, respectively, $\bar{d}_h$ and $\bar{d}_s$; the relative variances of the domain height distributions, $\sigma_h/\bar{d}_h$ and $\sigma_s/\bar{d}_s$; and the heterogeneity or skewing parameter, σ_H.

Considering our earlier study on the same set of data,[6] we expect that several of the data sets must be fitted using a model, which allows for the consideration of the presence of two components (taut and slack microfibrils).

Data Set To Be Fitted. The mathematical relation between the projected intensity $\{I\}_1(s_3)$ and the IDF $g_1(x_3)$ is a simple one. Therefore, the model can easily be adapted to fit either $\{I\}_1(s_3)$, the interference function $G_1(x_3)$, or the IDF $g_1(x_3)$.

3. Experimental Section

3.1. Sample Preparation and Pretreatment. The investigated material is a thermoplastic elastomer of multiblock poly(ether ester) (PEE) type. It is composed from poly(butylene terephthalate) (PBT) hard segment blocks and poly(ethylene glycol) (PEG) soft segment blocks. The latter have an average molecular weight of 1000 and a polydispersity of 1.3, as found by gel permeation chromatography. Such PEEs with a hard-to-soft ratio of 57/43 wt % was prepared by polycondensation.

By melt extrusion, isotropic bristles with a diameter of 2 mm were obtained, which after cooling to ambient temperature

were predrawn to 5 times their initial length. Finally stretched bristles with fixed ends were annealed for 6 h at 170 °C to obtain the anisotropic sample material for the X-ray scattering study.

Extended information on the sample preparation can be found in previously published work.[6]

3.2. Small-Angle X-ray Scattering Measurements. Synchrotron radiation (wavelength 0.154 nm) from the beamline A2 of the Hamburg Synchrotron Radiation Laboratory (HASYLAB) at DESY in Hamburg was applied. The distance between sample and detector was set to 2075 mm. Two-dimensional scattering patterns were registered on image plates. Exposure time was 2 min. From exposed image plates, an area of 900 × 900 pixels, each with a size of 176 μm × 176 μm, was read out on a Molecular Dynamics image plate scanner and used for evaluation. Valid scattering data were recorded in a circular region of reciprocal plane with a radius of $s_r = 0.25$ nm^{-1}.

A bristle was fixed in a straining stage with an initial free length between the clamps of 40 mm. Marks were painted on to the bristle in intervals of 5 mm. The strain rate was 30 mm/min. After the gap between the clamps was increased by 16 mm, the stage was stopped, and the scattering in the elongated state was recorded. Bristle thickness and distances between marks were measured during the changing of the image plate. Immediately after that, the movement direction of the stage was reversed, and the recording of a pattern "during relaxation" was started. We even tried to measure the relaxation of the structure by accumulating for 20 s only and taking a picture every minute, but we did not find observable differences among the four pictures taken, although the macroscopic shrinking process was still going on. After the image plate was changed, the next cycle was started, in which the final gap between the clamps was increased by another 16 mm. Empty scattering of the setup itself was recorded before and after the experimental series for later correction of the sample scattering.

Primary beam intensity was monitored during the experiment, and the absorption of the sample was measured using an ionization chamber mounted in the beam stop. Because of the uncertainty of the latter, we used instead the diameter of the bristle for normalization to a constant irradiated volume and represented the sample by a cylinder of constant height and measured diameter. This procedure is allowed because of the oblong shape of the primary beam, which intersects the fiber at right angles. Finally, all of the measured data were normalized to constant primary beam intensity and to constant irradiated volume. Empty scattering was subtracted after weighting by the sample absorption. Elongation

$$\epsilon = \frac{l - l_0}{l_0} \tag{6}$$

was computed from gaps between those marks which were enclosing the irradiated volume of the sample.

4. Data Evaluation

4.1. SAXS Data Processing. With respect to the procedure used in the earlier study,[6] data evaluation has been rewritten and extended,[24,25] now utilizing the powerful image processing library which come with the commercial scientific programming tool *Pv-wave*.[26] With minor modification, most of the procedures should run under *IDL* as well. *IDL* is closely related to *Pv-wave*. Sources and description are freely available on the web.[25] Because of the lack of information concerning the storage format used by the image plate scanner, at first we did not decompress the stored numbers by squaring them. This shortcoming led to strange results in a first, unpublished approach toward a quantitative analysis and is inherent to all data presented in the qualitative paper.[6] Fortunately, because we have only interpreted peak positions since then, it does not affect the results published earlier but only the shape of the curves presented in Figure 2 of that paper.

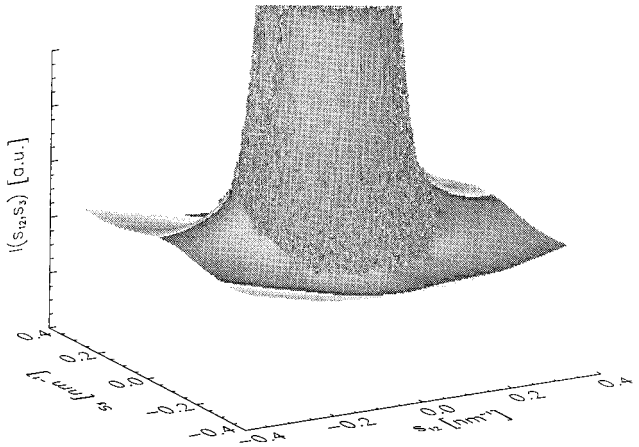

Figure 3. Extrapolation of an apron (smooth surface) to the measured SAXS intensity of the PEE sample elongated at $\epsilon = 1.1$.

Every sample pattern and empty pattern was properly decompressed, aligned, and normalized before further processing. Then, the empty pattern background was subtracted. Blind areas on the detector were identified utilizing a discriminating mask. After that, those regions were enlarged along their edges using the "erode" operator well-known in image processing. Now part of the missing data could be filled from the recorded data using the inherent symmetry of fiber patterns.

Finally, in the image, there remain a central blind spot and an outer dark area. In an ideal scattering pattern, both areas can be minimized by choosing a small beam stop, a relatively short sample-to-detector distance, and a wide vacuum tube. Bearing in mind a quantitative analysis of the scattering pattern, the necessity of having data from a wide area in the reciprocal plane arises from the fact that integrals have to be computed, and these must be extended virtually to infinity.

Concerning the central spot, the region was filled utilizing the 2D extrapolation procedure *RADBF* built into *Pv-wave*. This does not affect the results of the data evaluation, because not even part of a significant peak was hidden behind the beam stop.

Concerning the outer dark area, an apron (cf. Figure 3) was extrapolated again using *RADBF*, thus extending the usable area to a square with an edge length of 0.8 nm^{-1}. Because doing so modifies the background in projected curves, the implications of this extrapolation had to be tested thoroughly. At first, the extrapolated apron appears to be reasonable: it shows the expected minimum of the scattering intensity between small- and wide-angle scattering and swings up after that.

4.2. Projections. The projected intensity $\{I\}_1(s_3)$ now was calculated by use of eq 1.

4.3. Nonideal Two-Phase System. The first step of data analysis with respect to structural features is the search for Porod's law. By allowing for short-range fluctuations of the electron density (fluctuation background I_{Fl}) and a finite width of the transition zone between the hard and the soft domain phase (width of transition zone w_t), we allow the observed structure to be imperfect.[7]

We have chosen the fluctuation background I_{Fl} to be a constant, although there is good reason to consider a polynomial in even powers of s_3.[27] This choice has been made for practical reasons, because a more complicated method would require one to measure the background of the fiber scattering with high accuracy in the far-ranging vicinity of the observed reflections.

Figure 4 shows $\{I\}_1(s_3)$ in a plot that linearizes the Porod region according to eq 4. In this plot, I_{Fl} is varied until the Porod interval is at maximum length. Then, the width of the transition zone, w_t, is computed from the slope and the Porod

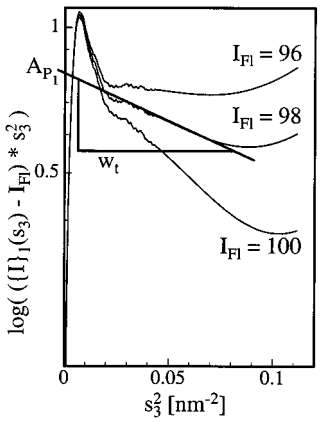

Figure 4. Porod's law and the consideration of the imperfect two-phase system in a plot which linearizes the Porod law region. The shape of the curve for various values of the fluctuation background I_{Fl} is indicated. The width of the transition zone, w_t, is computed from the slope and the Porod asymptote, A_{P_1} from the intercept of the Porod line. The PEE sample elongated at $\epsilon = 1.1$.

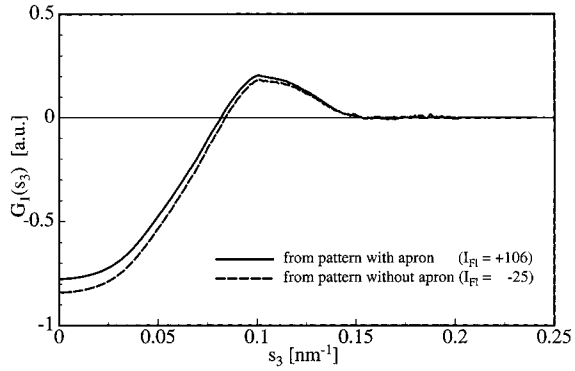

Figure 5. Effect of apron extrapolation for the sample in elongated state at $\epsilon = 1.1$. The interference functions $G_1(s)$ are computed from a SAXS pattern with extrapolated apron (solid line) and without consideration of extrapolated data (broken line).

asymptote, A_{P_1}, from the intercept of the Porod line. Intervals of confidence are estimated from this plot by varying I_{Fl}.

4.4. Interference Function and IDF. By using eq 4, the interference function can now be computed. It is smoothed using spline functions and a natural smoothing parameter, as has been described previously[8] and then transformed into real space by use of eq 5 yielding the IDF $g_1(x_3)$.

4.5. Implications of the Extrapolated Apron. Figure 5 shows an example of the effect of the extrapolated apron on the obtained interference function. If no apron is extrapolated prior to projection, straightening the Porod region requires addition to the background instead of subtraction from it. Consequently, slope w_t and intercept A_{P_1} of the regression line in Figure 4 become a function of the missing information. Nevertheless, when interference functions are compared; Figure 5 shows that the difference should not cause great concern. A comparison of model fits shows that $\bar{d}_h$ and $\bar{d}_s$, the average domain heights of the hard and the soft domain phase, are not affected by the missing data in the projection. On the other hand, $\sigma_h/\bar{d}_h$ and $\sigma_s/\bar{d}_s$, the widths of the distributions, yield scattered values without any sense. The same is found for the values of I_{Fl}, w_t, and A_{P_1}.

4.6. Model Fits. Model functions are fitted using the "simplex" algorithm for nonlinear regression. Detailed description has been published earlier,[8,28] and programs are freely accessible.[25] Examples of fits on $g_1(x_3)$ are presented in Figure 6. For zero and high elongations, a one-component model suffices. However, at medium elongation, we observe patterns with two differing long periods (cf. Figure 9), which consequently can only be fitted by a model function which supplies two types of microfibrillar components. The one-component model has 6 parameters to be fitted, and the two-component model has 12.

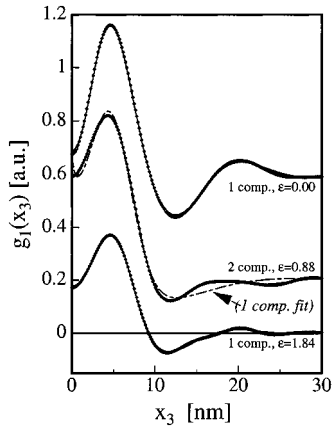

Figure 6. Examples of model function fits to interface distribution functions $g_1(x_3)$. Symbols represent data from the PEE sample in the elongated state at several elongations ϵ. Solid lines show the best fit. At medium elongation, one observes two kinds of long periods in the scattering pattern and fitting is possible by a two-component model only.

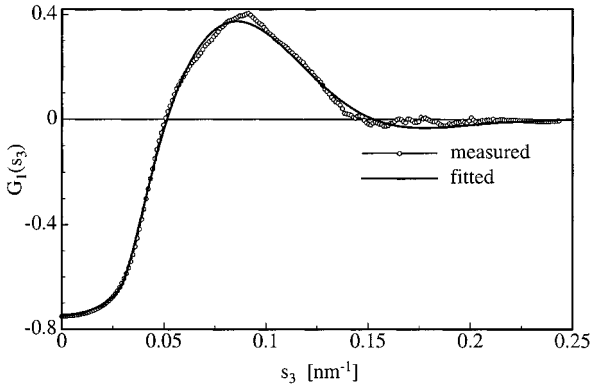

Figure 7. Fit on the interference function. Single-component model fit for the elongated sample at $\epsilon = 0.68$. This is the last elongation in the low elongation interval for which a single-component model gives reasonable parameters.

Figure 6 shows measured IDFs and the model fits in a stack plot. The quality of the fits is excellent. On a Pentium-100 computer, the minimum is found after approximately 1 h.

As has been indicated above, it is also possible to establish the model function for use directly with the interference function, $G_1(s_3)$, or even the projected intensity of an ideal two-phase system, $\{I\}_{1,id}(s_3)$. We did not succeed in fitting the intensity curves directly. Parameters drift in parameter space, and convergence is extremely slow.

On the other hand, there are cases where a fit on $G_1(s_3)$ proves feasible. Nevertheless, in contrast to fits on $g_1(x_3)$, two-component models converge extremely slowly, and even one-component models give strange results if the fits on $g_1(x_3)$ indicate that two strong components are present. If we confine ourselves to a one-component model, a high-quality fit can be performed on unsmoothed $G_1(s_3)$ curves. This fit reproduces the parameter values found in the corresponding fit of the corresponding $g_1(x_3)$ curves. The worst of the fits is shown in Figure 7.

It is the nature of fits in reciprocal space that they are extremely sensitive to long-range order, whereas the data in physical space are sensitive to short-range correlations only and faint long-range correlations are ignored. This principal feature causes fitting on scattering intensity or interference function to become a strenuous task and is reflected in the fact that to fit the interference function 115 distance distribu-

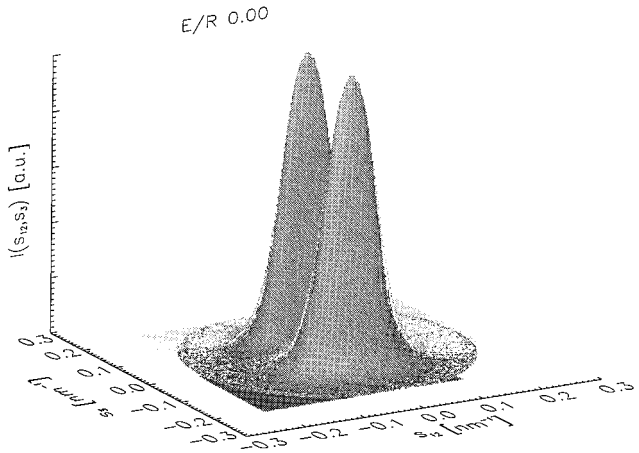

Figure 8. SAXS pattern of the original PEE fiber before starting the elongation cycles.

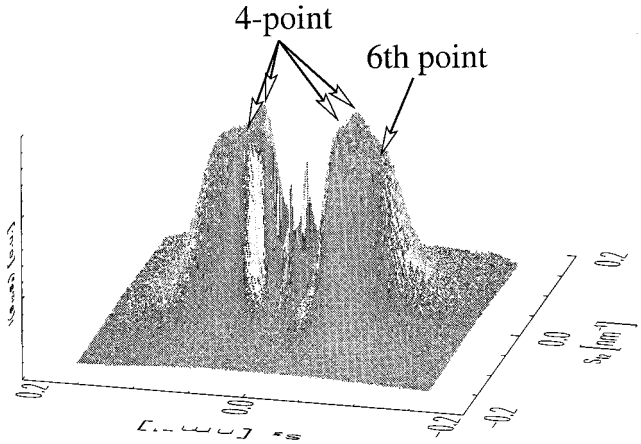

Figure 9. SAXS pattern of the PEE sample at an elongation of $\epsilon = 0.88$. The four peaks of the four-point pattern result in the first longitudinal long period. The second long period (slack fibrils) is in the fifth and sixth peak at the meridian.

tions $h_i(x_3)$ had to be accumulated. Doing so avoids artificial wiggling of the model function in the vicinity of 0. The necessity to consider many terms of the series slows down the regression considerably. Taking an upper limit of 55 distance distributions and blanking out the wiggling zone ($0 < s_3 < 0.025$ nm^{-1}) yields the same result in a much shorter time (30 min). On the other hand, for a fit on $g_1(x_3)$, it is generally sufficient sum up the first 25 distance distributions.

5. Results and Discussion

5.1. General Results. *Scattering Patterns.* Most of the scattering patterns have been published previously[6] in a 2D colorized representation. Thus, here it may suffice to present only three patterns. Figure 8 shows the SAXS pattern of the original PEE bristle before starting the elongation cycles. Because of the predrawing, it is highly oriented. Most of the extrapolated apron is not displayed.

Figure 9 shows the SAXS pattern of the PEE sample at an elongation of $\epsilon = 0.88$. The innermost strong peaks are split about the meridian ("4-point") and previously[6] have been attributed to an ensemble of taut microfibrils with lateral correlation ("macrolattice"). At even higher scattering angles and centered on the meridian, there is the broad shoulder of a second reflection ("6th point"), which previously has been attributed to a component of slack microfibrils which no longer interact with the external strain.

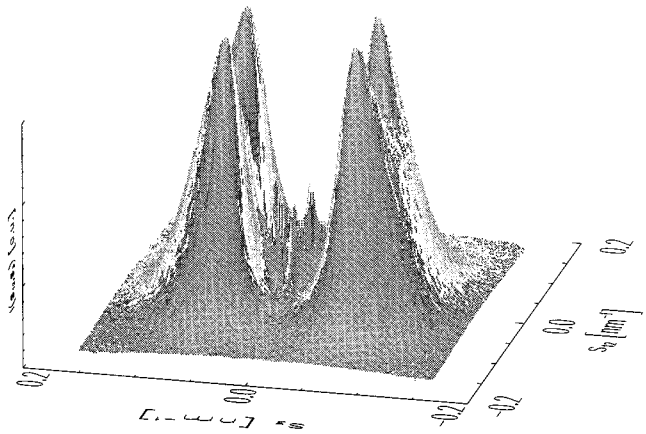

Figure 10. SAXS pattern of the PEE sample during relaxation from an elongation of $\epsilon = 0.88$. The four-point peaks have moved outward and are sharper now.

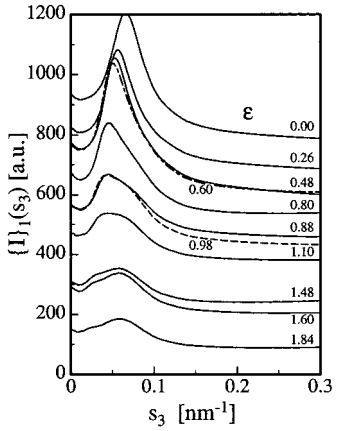

Figure 11. One-dimensional scattering curves $\{I\}_1(s_3)$ obtained by projection of scattering patterns onto the fiber direction. Curves are labeled with the elongation ϵ and stacked with an offset proportional to ϵ. Data from PEE sample in the elongated state.

Figure 10 shows the SAXS pattern of the PEE sample during relaxation from an elongation of $\epsilon = 0.88$. Because of the relaxation of the macrolattice its "4-point reflection" moves outward.

Projections. Data preprocessing, especially the extrapolation of an apron to the vicinity of the recorded pattern, has been described in Data Evaluation.

Figure 11 shows projected scattering intensities $\{I\}_1(s_3)$ of patterns related to the sample in elongated state. There is no visual difference between curves obtained from scattering patterns with or without extrapolated apron. Only the background and the slope of the curve in the Porod region are affected, as has been described in Data Evaluation.

Parameters of the Real Two-Phase System. Figure 12 shows the parameters determined during the search for Porod's law (cf. Figure 4). Three samples ($0.6 \le \epsilon \le 0.8$) show an elevated fluctuation background I_{Fl}, whereas a smooth master curve might be drawn through the other data points. Values for the interfacial width, w_t, scatter about values between 0.5 and 2.5 nm. This reflects the fact that SAXS, in general, is not the method to determine precise values of w_t. The Porod's asymptote, A_{P_1}, remains constant up to an elongation of $\epsilon = 0.6$ and decays in the further course, indicating a destruction of the two-phase structure.

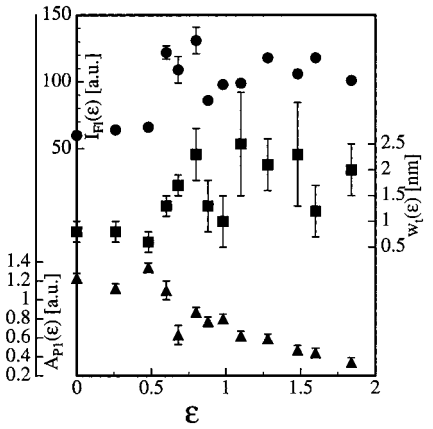

Figure 12. Parameters obtainable from the regression line in Figure 4: fluctuation background, I_{Fl}, width of phase transition region, w_t, and Porod's asymptote, A_{P_1}. Error bars are estimated from variation of the fluctuation background. Some systematic errors have not been considered but may arise from the normalization to constant irradiated volume and from some arbitrariness in the extrapolation of the apron (cf. Figure 3).

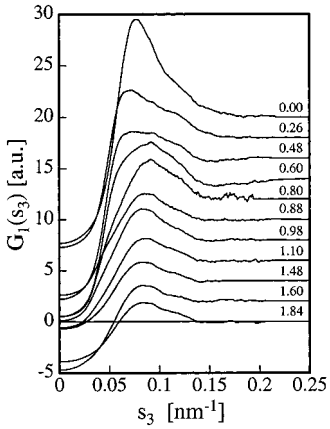

Figure 13. Interference functions $G_1(s_3)$ computed from the projected scattering intensity $\{I\}_1(s_3)$. PEE sample in the elongated state. Elongation ϵ is denoted as a legend to the curves stacked with constant offset.

From the pattern series recorded during sample relaxation, we get scattered data for the fluctuation background as well. This might be caused by the fact that we observe a dynamic system.

Interference Functions. Figure 13 shows a set of interference functions, $G_1(s_3)$, computed from the projected scattering intensity, $\{I\}_1(s_3)$, using eq 4. Data are from the PEE sample in the elongated state. The curves from the set during relaxation are not presented, because it is difficult to interpret these curves directly.

Interface Distribution Functions. According to eq 5, $g_1(x_3)$ curves have been computed from the interference functions. A set of such interface distribution functions is presented in Figure 14. The first minimum in these curves is related to the long period of the microfibrillar stack. Both of the domain height distributions are superimposed in the first maximum. A positive intercept indicates roughness of the domain surface.

5.2. Two-Phase Structure in Elongated State. *Average Domain Heights Determined from Model Fits.* The general result of a one-component (or a two-component) fit are two (or four) domain height distributions, each characterized by norm, mean, variance, and skewness. We thus determine how many domain heights

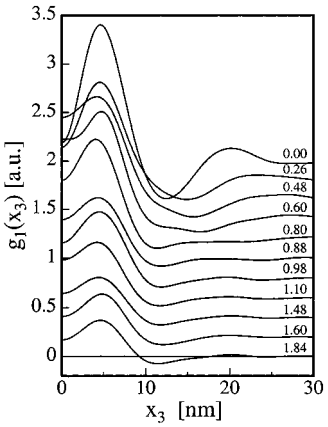

Figure 14. Interface distribution functions $g_1(x_3)$ computed from interference functions $G_1(s_3)$. PEE sample in the elongated state. Elongation ϵ is denoted as a legend to the curves stacked with constant offset.

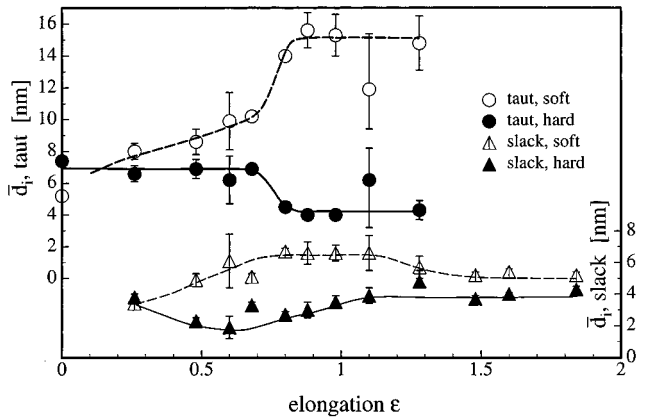

Figure 15. Average domain heights of taut (top, left scale) and slack (bottom, right scale) microfibrillar components as a function of elongation ϵ, as determined from one- and two-component fits, respectively. Elongated PEE sample. Fits performed on $g_1(x_3)$.

we observe (cf. values of A_{P_1} in Figure 12), what the value of the mean domain height is, how wide the domain height distribution is, and if this distribution is asymmetric.

In Figure 15, the determined average domain heights of soft and hard domains are presented. Although in principle the assignment of soft and hard domain heights is ambiguous, the interaction of the domain height distribution with external strain gives enough information to identify each distribution uniquely. An immediate result of this identification is that the volume fraction of hard domains in the original sample,

$$\phi_h = \frac{\bar{d}_h}{\bar{d}_h + \bar{d}_s} \tag{7}$$

can be computed from its average hard domain height, $\bar{d}_h = 7.4$ nm, as well as the average soft domain height, $\bar{d}_s$. The computed value of $\phi_h = 0.59$ is close to the hard-to-soft segment ratio of the polymer. We know that such agreement cannot be expected, because there are many structural features which have been discussed in the literature in order to predict or to explain deviations.

At medium elongation in the series from the elongated sample, we observe two kinds of microfibrils. The taut component (Figure 15, top) elastically interacts with the

external strain, whereas the slack component (Figure 15, bottom) collects the "waste" from microfibrils, which are no longer connected to the surrounding elastic network and remain in the relaxed state.

In the taut microfibrils at low elongations, soft domain heights start to grow continuously as a function of external elongation. The internal elongation of these soft domains is much higher than the elongation externally applied, which is a necessity because of the rigid nature of the hard domains filling the elastic network. Nevertheless, the average long period

$$L = \bar{d}_h + \bar{d}_s$$

of the taut component increases slower than external elongation ϵ. Let us study the internal elongation in more depth. Plotting long period versus external elongation ϵ for the first five scattering patterns, one finds a linear relationship and determines that the internal elongation of the long period,

$$\epsilon_L = 0.51\epsilon$$

is only half of the external elongation. This finding is in favor of a local irreversibility from the very beginning of the straining process. Let us now consider the average soft domain heights, $\bar{d}_s$. By plotting soft domain height versus ϵ, a quadratic relation appears to be appropriate. The fit results in the equation

$$\bar{d}_s(\epsilon) = (5.3 + 10\epsilon - 4.3\epsilon^2)\ \text{nm} \qquad (9)$$

and we deduce that the average initial internal elongation of the soft domains,

$$\epsilon_{s_0} = \frac{10}{5.3}\epsilon = 0.9\epsilon$$

is almost double the external elongation. On the other hand, at $\epsilon = 0.7$ just before the hard domains fail,

$$\epsilon_{s_{0.7}} = \frac{10 - 2 \times 4.3 \times 0.7}{5.3}\epsilon = 0.75\epsilon$$

the increase of the elastic domain heights compensates only three-quarters of the increase in external elongation.

Beyond an elongation of $\epsilon = 0.7$, we observe a sudden increase of the average soft domain height and a corresponding decrease of the hard domain height. We will discuss this phenomenon later.

Concerning the slack component, we observe that up to an elongation of $\epsilon = 0.6$ the average hard domain height decreases. This could be explained as the falling down of microfibrils (especially those with very short domains) into the slack component. In a similar manner, other variations of average values can be interpreted, but stronger evidence can be given when considering the domain height distributions as a whole.

Taut Components: Domain Height Distributions. As has been pointed out above, mean values do not suffice to describe the scattering and the structure. Only after statistics has been accounted for can the scattering data be fitted. Because the presentation of multicolumn tables appears to be somewhat awkward, we have chosen to plot the domain height distributions as a function of strain and then to discuss the findings in a qualitative manner.

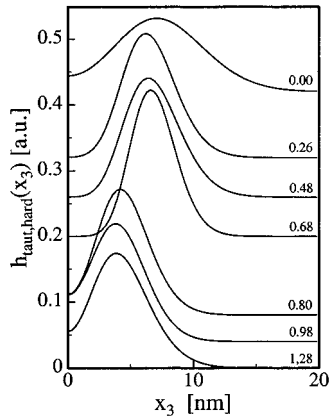

Figure 16. Height distributions of the hard domains in the taut microfibrillar component as reconstructed from the structural parameters of the fits. PEE in the elongated state. Curves are stacked and labeled with the elongation ϵ.

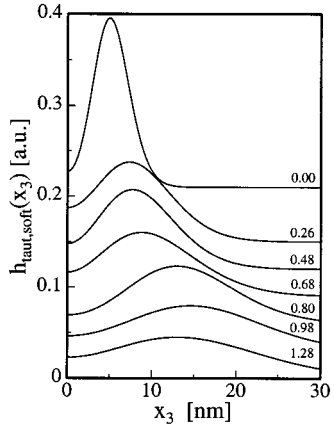

Figure 17. Height distributions of the soft domains in the taut microfibrillar component as reconstructed from the structural parameters of the fits. PEE in the elongated state. Curves are stacked and labeled with the elongation ϵ.

Figure 16 shows height distributions of the hard domains in the taut component. We observe that during the initial stages of straining the medium height domains are the most stable ones. By loss of tall and tiny hard domains to the slack component, the height distribution narrows considerably. Thus a material with a narrow distribution of hard domain heights would probably be a more perfect elastomer. Such an observation can be explained as the preferential detachment of hard segments of tie molecules connecting different microfibrils from tall or tiny hard domains. Such a mechanism slackens the elastic network.

After an elongation of $\epsilon = 0.7$ every hard domain appears to lose almost half of its height to the soft domain heights. This observation can be explained as the pulling out of tie molecules connecting adjacent hard segments within the same microfibril from hard domains, which relieves the stress inside a microfibril by an irreversible process. Drawn-out hard segments then become part of the soft domain phase.

The height distributions of the soft domains are presented in Figure 17. As soon as the sample is elongated, the distribution becomes broad, reflecting inhomogeneous elasticity of the soft domains in the material. During the further process of straining, further broadening is observed. The sudden shift of the distribution at $\epsilon = 0.7$ has already been discussed.

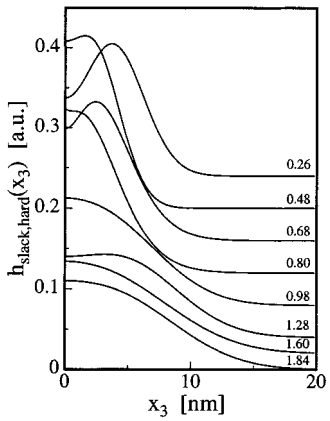

Figure 18. Height distributions of the hard domains in the slack microfibrillar component as reconstructed from the structural parameters of the fits. PEE in the elongated state. Curves are stacked and labeled with the elongation ϵ.

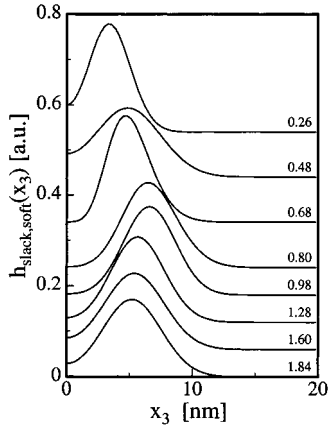

Figure 19. Height distributions of the soft domains in the slack microfibrillar component as reconstructed from the structural parameters of the fits. PEE in the elongated state. Curves are stacked and labeled with the elongation ϵ.

Slack Component: Domain Height Distributions. In the height distributions of the hard domains displayed in Figure 18, we find evidence for the explanation of the decrease of average hard domain height up to an elongation of $\epsilon = 0.6$. Here, we observe that the decrease is mainly caused from a strong increase of tiny hard domain fragments, which increasingly skew the distributions. On the other hand, for $\epsilon > 0.8$, we observe an increase of a fraction of tall hard domains in the reservoir of the slack component. Thus, up to an elongation of $\epsilon = 0.8$, the height distribution of slack hard domains is mainly fed by small, rough fragments. Beyond that, taller hard domains become slack, too.

As shown in Figure 19, the distribution of soft domain heights in the slack microfibrillar component is rather well-defined, similar to the width of the soft domain height distribution before stress has been applied. If we assume that the elasticity of the slack soft domains is not higher than that of the taut soft domains, we can deduce that this component, indeed, experiences low stress. When after $\epsilon = 0.7$ the hard domains in the taut microfibrils break down, even the slack component experiences some tension. During further elongation this strain is lost again.

5.3. Two-Phase Structure of the Relaxing Sample. Up to an elongation of $\epsilon = 0.8$, the interface distribution functions $g_1(x_3)$ can be fitted perfectly using a one-component model. For higher elongations, a two-component model takes into consideration an increasing component of damaged microfibrils. For elongations $\epsilon > 1.5$, the component made from intact microfibrils can no longer be detected. In Figure 20, the average domain heights of the intact microfibrillar component are shown. One observes that for relaxation from $\epsilon = 0.26$ the soft domain height ($\bar{d}_s \approx 4.3$ nm) is somewhat smaller than that for the original bristle ($\bar{d}_s \approx 5.2$ nm), whereas the average height of the hard domains ($\bar{d}_h \approx 7.5$ nm) is identical to that found for the unstrained sample ($\bar{d}_h \approx 7.4$ nm). To explain this finding, let us recall that the original bristle had been pretreated by predrawing and subsequent annealing with fixed ends.

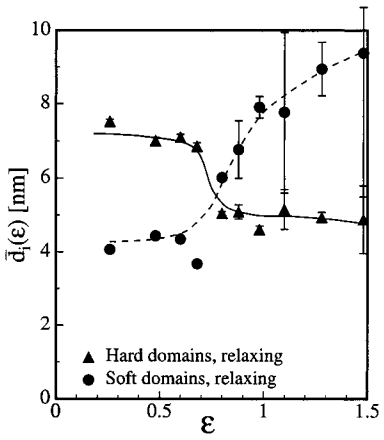

Figure 20. Average domain heights of the intact microfibrillar component. PEE sample relaxing from elongation ϵ. Fits performed on $g_1(x_3)$.

Average Domain Heights Determined from Model Fits. Figure 20 shows that up to $\epsilon = 0.7$ the intact microfibrillar component shows no remnant elongation, because hard and soft domain heights are almost constant. Nevertheless, a slight decrease of the hard domain height and a slight increase of the soft domain height can be observed. This observation supports a conclusion drawn in earlier work[29,30] that even in the early interval of straining hard domains are degraded by the pulling out of tie molecules, this being a process which decreases the degree of physical cross-linking.

At $\epsilon = 0.8$, we observe the breakdown of the hard domain height in the relaxing images, which is well-known from the elongated samples (cf. Figure 15). From now on, as a function of elongation, we observe a monotonic increase of the average soft domain height, while the component of intact microfibrils becomes weaker and weaker, resulting in an increase of the error of determination.

Structure of Intact Microfibrils. For the component made from intact microfibrils, Figure 21 shows the frequency distributions of hard domain heights during the relaxation from the indicated elongation. By comparison of Figures 15 and 20, we have already observed the identical behavior of the average hard domain heights. Now by comparison of Figures 21 and Figure 16, we observe that the frequency distributions of the heights as a whole look very similar. Thus, it is clear that the "taut component" in elongated state is identical to the "intact component" during sample relaxation.

Let us continue discussing the intact microfibrillar component but now turn to the frequency distributions of the soft domain heights (Figure 22). Although the mean soft domain height remains constant during the

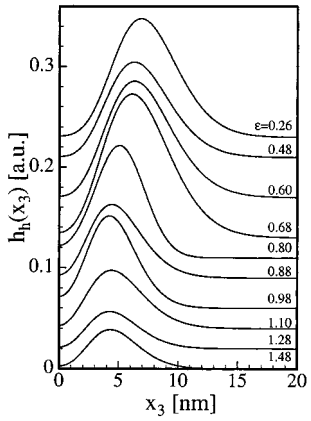

Figure 21. Height distributions $h_h(x_3)$ of the hard domains in the intact microfibrillar component as reconstructed from the structural parameters of the fits. PEE sample relaxing from elongation ϵ. Curves are stacked, labeled with the elongation, and normalized to their true weight in the fit.

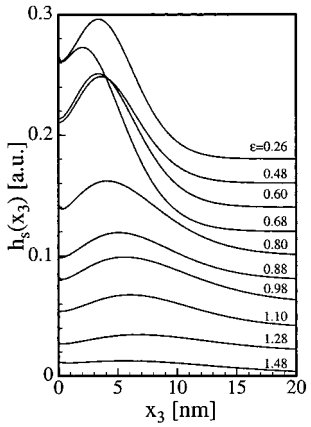

Figure 22. Height distributions $h_s(x_3)$ of the soft domains in the intact microfibrillar component as reconstructed from the structural parameters of the fits. PEE sample relaxing from elongation ϵ. Curves are stacked, labeled with the elongation, and normalized to their true weight in the fit.

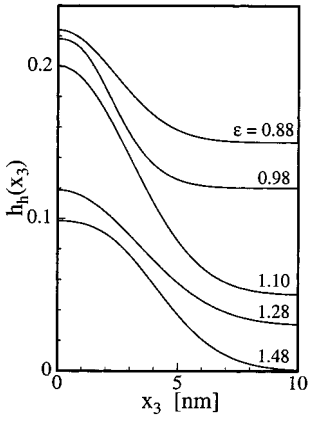

Figure 23. Height distributions $h_h(x_3)$ of the hard domains in the damaged microfibrillar component as reconstructed from the structural parameters of the fits. PEE sample relaxing from elongation ϵ. Curves are stacked, labeled with the elongation, and normalized to their true weight in the fit.

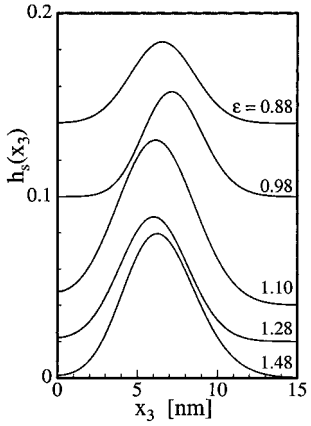

Figure 24. Height distributions $h_s(x_3)$ of the soft domains in the damaged microfibrillar component as reconstructed from the structural parameters of the fits. PEE sample relaxing from elongation ϵ. Curves are stacked, labeled with the elongation, and normalized to their true weight in the fit.

first four cycles, the shape of the distribution varies. Here, we observe an increase of very tiny soft domain heights, while the domain distribution broadens as a whole. After crossing the critical elongation at $\epsilon = 0.8$, the number of tiny soft domain heights decreases considerably. In the elongated state (Figure 17), similar behavior is found. We can explain such finding if we assume Young's modulus to vary as a function of initial soft domain height.

By comparison of the soft domain distributions from Figure 17 with those presented in Figure 22, we observe that at constant elongation the curves look similar concerning relative width and skewness. In comparison to the elongated state, the relaxing distributions, of course, are contracted about the x_3-axis.

Structure of the Damaged Microfibrillar Component. As mentioned above, beginning with $\epsilon = 0.88$, the data from the relaxing PEE sample can only be fitted if a second microfibrillar component is considered, which becomes stronger and stronger with increasing elongation and which is the only component remaining for $\epsilon > 1.48$. As shown in Figure 23, the hard domain heights of this component contain a considerable amount of fragments, while the distribution of soft domain heights (cf. Figure 24) is symmetrical and rather narrow. Comparing these distributions with the data from the sample in the elongated state (Figures 18 and 19) it becomes clear that the slack component from the elongated sample is identical to the damaged microfibrillar component found in the small-angle scattering of the relaxing sample.

Quantitative and Qualitative Analysis. Comparing the results from the quantitative analysis presented here with those from the qualitative analysis published previously,[6] we observe the same transitions in the domain height distributions that earlier were deduced from changes in the positions of the long period. The long periods computed from the quantitative analysis are somewhat smaller than those computed from the positions of peak maxima, as is to be expected because the structure exhibits a broad distribution of long periods. At $\epsilon = 0.6$, e.g., the long period determined from the quantitative analysis according to eq 8 gives a value of $L = 16$ nm, whereas from the peak position, we determine a value of 19 nm.

6. Conclusions

As has been shown in this study, a prerequisite for a successful quantitative analysis of small-angle scattering patterns with fiber symmetry is the careful choice of a small beam stop, a wide vacuum tube, and rather a short distance between sample and detector. By doing

so, one can hope to register not only all of the reflections with the required accuracy and spatial resolution but also the important background scattering, including the increase of scattering intensity toward the WAXS regime.

Then, a quantitative analysis of the two-phase structure becomes feasible. For a thermoplastic elastomer both in patterns from the elongated state and during sample relaxation, respectively, we identify the same two structural components, namely, an intact microfibrillar network which directly interacts with the external strain and an ensemble of damaged microfibrils, in which the soft domain height is well-defined. Each of these components has been described by a small set of parameters that model the frequency distributions of domain heights in the fibrous material. The reader now may ask how reliably such frequency distributions presented in Figures 16−19 and 21−24 can be reproduced. The answer can be estimated by comparing the results with each other. By use of the same straightforward method, 26 different scattering patterns have been projected, analyzed and fitted. The visualization of these fits shows a clear correlation as a function of elongation and a trend which is closely coupled to the features directly extracted from the 2D scattering images. Thus, the estimated reliability is high. If, on the other hand, we would modify the structural model, the domain height distributions might look different; e.g., let us assume there were reasons to introduce an additional distribution centered on the origin, then every domain height distribution would become narrower, but the general trend as discussed here would not be changed.

We expect that quantitative investigations such as the present one may help to match parameters in a mechanical model for filled elastic networks, concerning elastic and viscous parameters, as well as for the investigation of strain hardening. The proposed method of data analysis is not restricted to studies of elastomers. Beyond that, it can be applied to any material with pronounced fiber orientation and a two-phase structure.

Acknowledgment. This study has been supported by the Bilateral Cooperation Program between the University of Hamburg, Germany, and the University of Sofia, Bulgaria, which is funded by the DAAD (German Academic Exchange Service). SAXS investigations have been supported by HASYLAB Hamburg.

References and Notes

(1) Bonart, R. *Kolloid Z. Z. Polym.* **1966**, *211*, 14.
(2) Statton, W. O. *Z. Kristallogr.* **1968**, *127*, 229.
(3) Peterlin, A. *Text. Res. J.* **1972**, *42* (1), 20.
(4) Rudolf, P. R.; Landes, B. G. *Spectroscopy (Eugene, Oreg.)* **1994**, *9* (6), 22.
(5) Stribeck, N. *J. Polym. Sci., Part B: Polym. Phys.* **1998**, in press.
(6) Stribeck, N.; Sapoundjieva, D.; Denchev, Z.; Apostolov, A. A.; Zachmann, H. G.; Stamm, M.; Fakirov, S. *Macromolecules* **1997**, *30* (5), 1329.
(7) Ruland, W. *J. Appl. Cryst.* **1971**, *4*, 71.
(8) Stribeck, N. *Colloid Polym. Sci.* **1993**, *271* (11), 1007.
(9) Ruland, W. *Colloid Polym. Sci.* **1977**, *255*, 417.
(10) Stribeck, N.; Ruland, W. *J. Appl. Cryst.* **1978**, *11*, 535.
(11) Hermans, J. J. *Recl. Trav. Chim. Pays-Bas* **1944**, *63*, 211.
(12) Porod, G. *Kolloid-Z.* **1951**, *124*, 83.
(13) Strobl, G. R.; Müller, N. *J. Polym. Sci., Part B: Polym. Phys.* **1973**, *11*, 1219.
(14) Murthy, N. S.; Bednarczyk, C.; Moore, R. A. F.; Grubb, D. T. *J. Polym. Sci., Part B: Polym. Phys.* **1996**, *34* (5), 821.
(15) Murthy, N. S.; Zero, K.; Grubb, D. T. *Polymer* **1997**, *38* (5), 1021.
(16) Ruland, W. *Colloid Polym. Sci.* **1977**, *255*, 833.
(17) Vonk, C. G.; Kortleve, G. *Kolloid-Z. Z. Polym.* **1967**, *220*, 19.
(18) Kortleve, G.; Vonk, C. G. *Kolloid-Z. Z. Polym.* **1968**, *255*, 124.
(19) Santa Cruz, C.; Stribeck, N.; Zachmann, H. G.; Baltà Calleja, F. J. *Macromolecules* **1991**, *24*, 5980.
(20) Goderis, B. DSM Corp., The Netherlands. Private Communication, 1998.
(21) Ruland, W. *Colloid Polym. Sci.* **1978**, *256*, 932.
(22) Stribeck, N.; Reimers, C.; Ghioca, P.; Buzdugan, E. *J. Polym. Sci., Part B: Polym. Phys.* **1998**, *36*, 1423.
(23) Brämer, R. *Colloid Polym. Sci.* **1974**, *252*, 504.
(24) Stribeck, N. *Fibre Diffr. Rev.* **1997**, *6*, 20.
(25) Stribeck, N. Web Page. http://www.chemie.uni-hamburg.de/tmc/stribeck/.
(26) *Pv-wave*, version 6.10; Visual Numerics, Inc.: Boulder, Colorado, 1990−1997.
(27) Wiegand, W.; Ruland, W. *Progr. Colloid Polym. Sci.* **1979**, *66*, 355.
(28) Stribeck, N. *Colloid Polym. Sci.* **1989**, *267*, 301.
(29) Fakirov, S.; Fakirov, C.; Fischer, E. W.; Stamm, M. *Polymer* **1991**, *32* (7), 1173.
(30) Fakirov, S.; Fakirov, C.; Fischer, E. W.; Stamm, M. *Polymer* **1992**, *33* (18), 3818.

MA9818477